nature energy

Article

https://doi.org/10.1038/s41560-024-01589-5

Geometric design of Cu_2Se-based thermoelectric materials for enhancing power generation

Received: 9 August 2023

Accepted: 28 June 2024

Published online: 19 July 2024

Check for updates

Seungjun Choo[1,10], Jungsoo Lee[1,10], Bengisu Şişik[2], Sung-Jin Jung[3,4], Keonkuk Kim[1], Seong Eun Yang[1], Seungki Jo[5], Changhyeon Nam[6], Sangjoon Ahn[6], Ho Seong Lee[7], Han Gi Chae[8], Seong Keun Kim[4,9], Saniya LeBlanc[2] ✉ & Jae Sung Son[1] ✉

Waste heat, an abundant energy source generated by both industries and nature, has the potential to be harnessed into electricity via thermoelectric power generation. The performance of thermoelectric modules, typically composed of cuboid-shaped materials, depends on both the materials' intrinsic properties and the temperature difference created. Despite significant advancements in the development of efficient materials, macroscopic thermal designs capable of accommodating larger temperature differences have been largely underexplored because of the challenges associated with processing bulk thermoelectric materials. Here we present the design strategy for Cu_2Se thermoelectric materials for high-temperature power generation using a combination of finite element modelling and 3D printing. The macroscopic geometries and microscopic defects in Cu_2Se materials are precisely engineered by optimizing the 3D printing and post-treatment processes, leading to notable enhancements in the material efficiency and temperature difference across legs, where the hourglass geometry exhibits maximized output powers and efficiencies. The proposed approach paves the way for designing efficient thermoelectric power generators.

Global energy consumption is growing rapidly, and there is an urgent need for sustainable and renewable energy sources to address fossil fuel depletion and environmental pollution[1–3]. Waste heat is one of the most relevant renewable sources because it is generated by numerous systems, including automobiles, ships, power plants and industrial plants of oil refineries and steelmaking[4–6]. Thermoelectric (TE) power generation offers a unique solution for the reliable and sustainable recovery of dissipated waste heat because it enables the direct conversion of heat to electricity without environmental pollution[7–10]. The energy conversion efficiency of TE devices depends on the efficiency of the TE material and the temperature difference across the TE devices[9–12]. Achieving a large temperature gradient across the TE device and ultimately maximizing energy conversion efficiency requires the device-level design of TE generator[13,14]. The key design parameters in the conventional cuboid TE leg-based devices include the length and aspect ratio of the cuboid legs and their fill factor[15–20]. Another important design strategy can involve the optimization of non-cuboid geometries for individual TE legs. This strategy offers an additional level of control over thermal transport and enables the creation of larger temperature differences compared with cuboid-shaped legs[21–27]. Although several simulation studies on non-cuboid geometries of TE legs have been reported in some specific conditions, there has been a scarcity of the experimental validation combined with a comprehensive design for power generation in non-cuboid TE legs. This limitation is attributed to the challenge

A full list of affiliations appears at the end of the paper. ✉e-mail: sleblanc@gwu.edu; sonjs@postech.ac.kr

https://doi.org/10.1038/s41560-024-01589-5

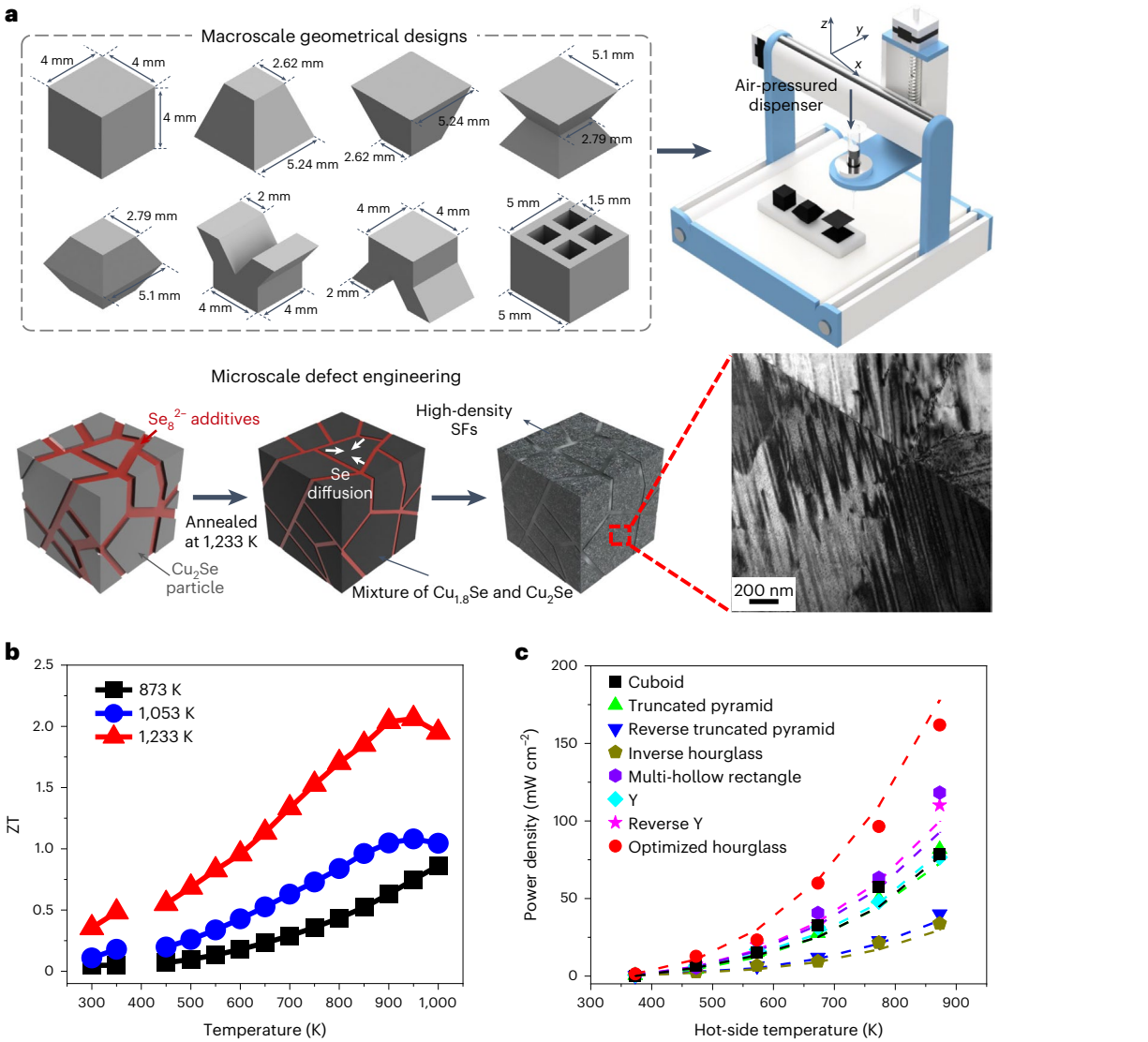

Fig. 1 | Geometric designs and defect engineering of 3D-printed Cu_2Se. **a**, A schematic illustrating defect engineering and geometric designs of 3D-printed Cu_2Se for a high-output power TE material. The TE leg designs had identical volumes and heights. **b**, The *ZT* values of 3D-printed Cu_2Se. **c**, Power densities of 3D-printed Cu_2Se devices as a function of hot-side temperatures in the range of 323–873 K. In **c**, the points represent the values obtained from direct measurements, while the dashed lines indicate the values predicted through numerical simulations by finite element method, demonstrating a high degree of similarity and validating the experiment's outcomes.

of fabricating materials with complex geometries by the conventional metallurgical manufacturing process.

Recently, three-dimensional (3D) printing has emerged as a promising manufacturing process for TE materials and offers the potential to customize TE legs into specific geometries[28–35]. However, this technology is still in the development phase, and further advancements are necessary to meet the manufacturing criteria for TE materials. These criteria include ensuring structural fidelity and achieving a high TE figure of merit (*ZT*) in the printed products. The reported efficiencies of 3D-printed TE materials have generally been lower than those achieved through traditional fabrication methods, such as hot pressing or melting[28,36]. Enhancing the TE properties of materials requires the precise engineering of atomic defects and microstructures during the fabrication stage[37,38]. However, this presents a challenge in the 3D printing process because the incorporation of additives or modifications to the microstructure can adversely affect the rheological properties of the particle-based inks and compromise the printability of the resulting 3D structures.

Here, we present a design strategy for determining the best geometry of TE legs for high-temperature power generation of Cu_2Se through 3D finite element model (FEM) simulations and experimental validation of the design using an extrusion-based 3D printing process. Liquid-like materials of Cu_2Se arguably represent high-temperature TE materials owing to their high efficiencies resulting from their extremely low thermal conductivities[39–44]. We conducted numerical simulations to evaluate the power generation of eight different geometries of the Cu_2Se TE legs under diverse working conditions and further optimized the geometric parameters of the best-performing hourglass geometry. Moreover, the controlled liquid-phase sintering and Se evaporation of the printed Cu_2Se products allowed the defect formation of high-density stacking faults (SFs) and the resulting dislocations. These defects reduced the thermal conductivity of Cu_2Se and consequently enhanced the *ZT* values up to 2.0 at 950 K. To validate our designs, we fabricated and comparatively evaluated the power-generating power performances of the 3D-printed Cu_2Se legs. The hourglass-shaped TE leg generated substantially higher power and efficiency compared

with those of the conventional cuboid-shaped TE material, experimentally validating our approach towards the maximization of power-generating performances of TE devices.

Results

Geometric design of TE legs

The overall design of Cu_2Se TE materials, focusing on macroscale geometry and microscale defects to enhance ZT values and output power density, is summarized in Fig. 1.

The maximum output power (P_{max}) of TE devices is defined using equation (1),

$$P_{max} = \frac{S^2\Delta T^2}{4R_{el}} = \frac{(SQR_{th})^2}{4R_{el}}, \quad (1)$$

where S is the Seebeck coefficient, R_{el} is the electrical resistance of a TE leg, and $\Delta T = QR_{th}$ is the created temperature difference, where Q is the heat flowing through a TE leg and R_{th} is the thermal resistance of a TE leg. To maximize P_{max} in this simple relation, the optimization of R_{el} and R_{th} is generally conducted with the parameter of the aspect ratio of a cuboid TE leg because they have a trade-off relationship with respect to the length and cross-sectional area of the TE leg. In the non-cuboid TE leg, R_{el} and R_{th} can be defined using equation (2),

$$R_{el} = \int_0^L \frac{dl}{\sigma A}, \quad R_{th} = \int_0^L \frac{dl}{kA} \quad (2)$$

where L is the vertical length, σ is the electrical conductivity, k is the thermal conductivity and A is the cross-sectional area of the TE leg[45]. The geometric parameter of $\int_0^L \frac{dl}{A}$ of the TE leg is present in equation (2). Because several factors affect the overall output power of a device, such as the temperature dependencies of σ and k, convection areas and conduction path, this geometric parameter could be more flexible and effective for maximizing P_{max} than the aspect ratio of a cuboid leg. For example, LeBlanc and coworkers investigated the influence of TE leg shapes by simulations, finding that the hourglass- and trapezoid-shaped TE legs generate more power than twice as much as the cuboid[27].

To design geometry of Cu_2Se TE legs, we developed a 3D FEM model for the eight different geometries of the TE legs and comparatively computed their R_{el}, ΔT, output voltage (V), P_{max} and efficiency (η) (Fig. 1a). We chose these geometries by considering the geometric parameters of $\int_0^L \frac{dl}{A}$, for which the selected geometries were varied (Supplementary Table 1), the conduction path (Y shape and reverse Y shape) or the holes in it (multi-hollow rectangle). Initially, we computed the power-generating performances of the single leg, wherein the TE leg is sandwiched between the top and bottom Cu electrodes and Ag paste solder, under various thermal environment conditions by varying the convection heat transfer coefficients (h) at both hot and cold sides with the ambient temperatures of 873 K and 300 K, respectively (Fig. 2a). This approach effectively encompasses the wide range of working conditions encountered in TE devices. Figure 2b–f illustrates the 3D plots of the relative properties of complex geometries to those of the cuboid (Supplementary Figs. 1 and 2). It was observed that a lower h on either the hot or cold side resulted in a predicted increase in ΔT for the hourglass, Y, reverse Y and multi-hollow rectangle, whereas a decrease in ΔT relative to the cuboid was anticipated for truncated pyramid, reverse truncated pyramid and inverse hourglass. With escalating h values on either side, the variations in relative ΔT within the complex geometries diminished, converging to a constant value at high h levels on both the hot and cold sides, consistent with a fixed ΔT condition. Correspondingly, the V mirrored the trends in ΔT. This result can be interpreted by the combined effect of the geometric parameters that determine the R_{th} of the leg, as well as the heating and cooling surface areas that determines the heat transfer rate at the hot side (Q_h) and cold side (Q_c), resulting in ΔT. The convective heat transfer rate (Q_{conv}) was defined by $Q_{conv} = hA\Delta T_{conv}$, where A and ΔT_{conv} are the exposed surface area and temperature difference between the solid and fluid medium. The R_{el} was generally found to be independent of the h as it is predominantly determined by the material's electrical conductivity, geometric parameters, contact resistance (R_c) and contact resistivity of 4.88×10^{-7} Ωm^2 (Supplementary Fig. 3)[46]. Owing to greater contact areas, the hourglass was projected to exhibit lower relative R_{el}. Owing to the superior ΔT and reduced R_c, the hourglass demonstrates a markedly enhanced performance in terms of P_{max} and η compared with all others in the entire ranges of h, on both the hot and cold sides.

In addition, we conducted the simulations under two specific working conditions: one comprising a fixed hot-side temperature (T_h) of 873 K and forced convection at the cold side, and the other comprising a fixed ΔT. These conditions correspond to the cut planes of the 3D plots in Fig. 2b–f, corresponding to the cold-side $h = 200$ W m^{-2} K^{-1} and the both-side $h = \infty$ W m^{-2} K^{-1}. The former condition holds relevance in real-world applications, where a TE device is applied to a hot reservoir and cooled using a heat sink. Conversely, the latter condition is commonly employed in the field of TE devices, enabling a straightforward comparative assessment of TE devices. Under the former condition (Fig. 2g), the hourglass and truncated pyramid with higher R_{th} and larger geometric parameter than those of the cuboid were expected to produce the higher ΔT. Meanwhile, the Y-shaped and reverse Y-shape legs with the same geometric parameter as the cuboid exhibited a slightly higher ΔT owing to a longer thermal conduction path. In contrast, the reverse truncated pyramid and inverse hourglass that have smaller cooling areas exhibited considerably lower ΔT and P_{max} values. Consequently, the hourglass, Y-shaped and reverse Y-shaped legs outperformed the cuboid in terms of P_{max} and η, with the hourglass design emerging as the most efficient. Despite higher ΔT expected in the truncated pyramid, its P_{max} and η were limited due to the large R_{el}.

Under the fixed ΔT condition ($h = \infty$ W m^{-2} K^{-1}), the impact of R_{th} and Seebeck voltage on the P_{max} is pre-determined by the fixed ΔT, rendering the P_{max} contingent solely on the R_{el}. The hourglass shows a remarkable enhancement in both P_{max} and η, considerably outperforming the cuboid (Fig. 2h). Moreover, the performances of the Y shape and reverse Y shape increased as well. These enhancements are attributed to the larger geometric parameters since those with greater R_{th} required less Q_h to establish the same ΔT. Thus, the reduction in P_{max} by R_{el} was offset by the lower Q_h, resulting in improved η. Additionally the increased contact areas reduce R_{el}, thereby boosting the efficiency.

Further, the standardization of the heating and cooling surface areas and the R_c, and the application of the design strategy to different materials, specifically BiSbTe, are discussed in Supplementary Discussions 1 and 2 (Supplementary Figs. 4–7). All the simulations show that the hourglass consistently outperformed other geometries in terms of P_{max} and η except under ideal fixed-temperature conditions without R_c.

Finally, the optimization for the area ratio (β/α) and the position of the centre neck (γ) was performed on the hourglass, where α, β and γ represent the area at the centre, the areas of the top and bottom surfaces, and the normalized position of the centre neck from the hot side in the range 0–1, respectively (Fig. 3a). With an increase in β/α to approximately 10, the ΔT and resulting V abruptly increased, while the R_{el} decreased (Fig. 3b,c and Supplementary Figs. 8 and 9). Above β/α of 12, all values were nearly saturated or changed slowly, but the P_{max} decreased owing to the increase in the R_{el}. Overall, the P_{max} was maximized at an area ratio of 11.65, at which the predicted V and P_{max} were 24% and 131% higher than those of the cuboid. The optimal value for γ was found to be 0.519, slightly below the centre with a β/α of 11.65.

https://doi.org/10.1038/s41560-024-01589-5

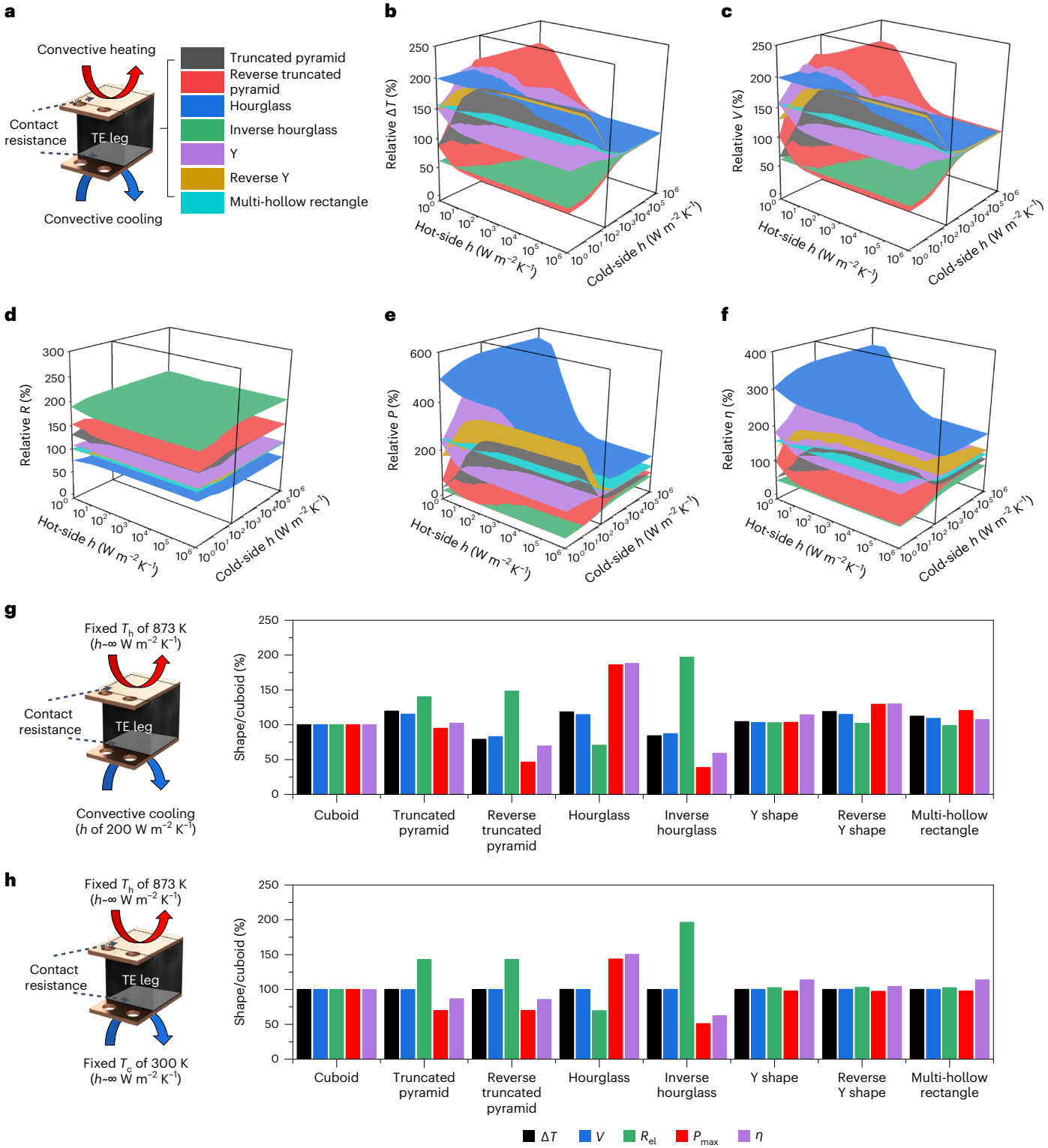

Fig. 2 | Cu_2Se TE leg designs. a, A schematic illustrating working condition of 3D-printed Cu_2Se TE device. **b**–**f**, The percentage of temperature difference (**b**), voltage (**c**), electrical resistance (**d**), output power (**e**) and efficiency (**f**) of eight different leg shapes compared with those of a cuboid-shaped leg under the diverse convection coefficient of the hot and cold sides. The vertical planes are the cut planes of the cold-side convection coefficient 200 W m^{-2} K^{-1}. **g**,**h**, Schemes illustrating the working conditions of the 3D-printed Cu_2Se TE device: the percentage of temperature difference, output voltage, electrical resistance, output power and efficiency of eight different leg shapes compared with those of a cuboid-shaped leg at the cut planes of the cold-side convection coefficient 200 W m^{-2} K^{-1} (**g**) and the infinite of convection coefficient of the hot and cold sides (**h**).

However, the marginal improvement of approximately 1% in the P_{max} was predicted compared with the base design with the γ of 0.5. Considering the 3D printing resolution, we chose the optimum hourglass with the β/α of 11.65 and γ of 0.5 for the experimental validation (Fig. 3c, inset). The optimization of the hourglass geometry is further discussed in Supplementary Discussions 3 and 4 (Supplementary Figs. 10–12).

https://doi.org/10.1038/s41560-024-01589-5

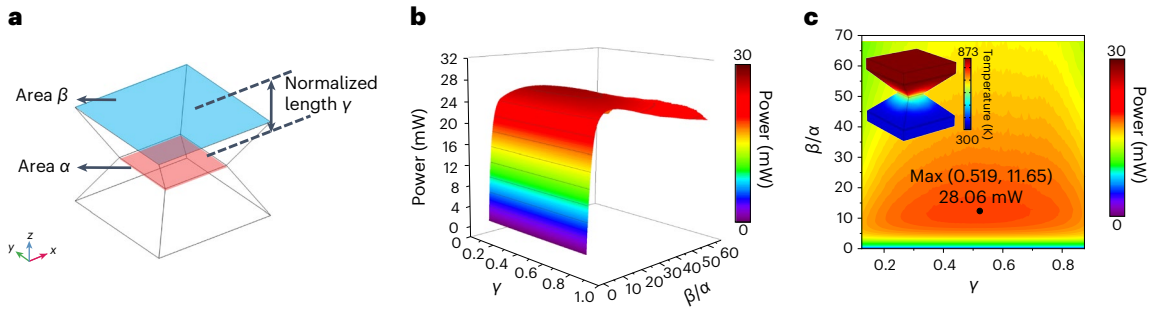

Fig. 3 | Optimization of the hourglass-shaped Cu_2Se TE leg. a, A schematic illustrating design variables of an hourglass-shaped Cu_2Se TE leg. **b**, The output power of the hourglass-shaped Cu_2Se TE leg as a function of the ratio of cross-sectional area (β/α) and the length of centre neck from the hot side (γ). **c**, Contour of output power and maximum point for power-generating performance. The inset indicates the temperature distribution of optimal hourglass-shaped Cu_2Se TE leg for power-generating performance.

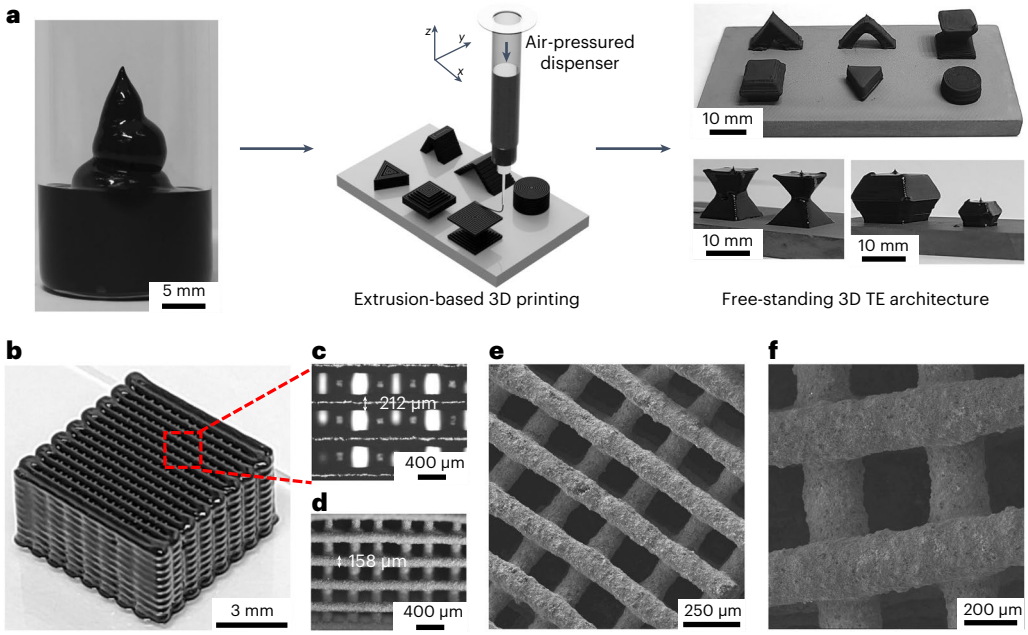

Fig. 4 | 3D printing of geometric-designed Cu_2Se TE materials. a, A schematic displaying the 3D printing process of the Cu_2Se free-standing shapes using all-inorganic Cu_2Se ink. **b**,**c**, A photograph (**b**) and optical microscopy (OM) image (**c**) of the as-printed 3D lattice structure constructed of layer-by-layer-deposited Cu_2Se ink filaments. **d**–**f**, OM (**d**) and low- (**e**) and high-magnification (**f**) SEM images of the sintered 3D Cu_2Se lattice.

3D printing of the geometrically designed Cu_2Se

To achieve ink-extrusion-based 3D printing of Cu_2Se, we formulated a Cu_2Se particle-based colloid ink with the desired viscoelasticity. Our group has previously reported the extrusion-based 3D printing of Cu_2Se inks whose rheological properties were tailored by the addition of Se_8^{2-} polyanions[33]. In the current study, we further increased the concentration of solutes in the glycerol solvent medium, resulting in a higher viscosity (Supplementary Fig. 13). This rheological modification improved the 3D printability of our inks to make them directly writable, which enabled us to build complex architectures, including hourglass, arch and lattice structures constructed by directly written filaments (Fig. 4a and Supplementary Movies 1–3). Optical microscopy and scanning electron microscopy (SEM) images of the printed filaments (Fig. 4b–f) show their smooth surface and uniform thickness. Moreover, after heat treatment at 1,233 K, the primary shape of the filament was preserved perfectly without structural distortion. Additionally, the as-printed filament had a diameter of approximately 210 μm while the sintered filament uniformly shrank to a diameter of approximately 160 μm after the heat treatment, indicating densification of the printed filament.

TE properties of the 3D-printed Cu_2Se

The use of Se_8^{2-} polyanions as rheology-modifying additives also promotes the sintering of Cu_2Se. Upon heat treatment, Se_8^{2-} polyanions are decomposed into the Se phase at ~140 °C among Cu_2Se particles (Supplementary Fig. 14) and induce the liquid-phase sintering of Cu_2Se particles due to the relatively low melting point of Se (~220 °C). We investigated the effect of sintering temperatures on the TE properties of samples (873, 1,053 and 1,233 K). The SEM images show that all samples sintered at 873, 1,053 and 1,233 K have well-fused grains with multiple pores in their microstructures, suggesting a sintering effect of the Se_8^{2-} polyanions (Supplementary Fig. 15)[28–33]. Also, excess Se polyanions allowed us to control the composition of $Cu_{2-x}Se$ because elemental Se gradually evaporates during sintering. X-ray diffraction (XRD) patterns of the samples sintered at 873, 1,053 and 1,233 K revealed that the $Cu_{1.8}Se$ phase mixed with the Cu_2Se phase was observed in the

sample sintered at 873 K, and the peaks of the $Cu_{1.8}Se$ phase progressively disappeared with increasing sintering temperature (Fig. 5a). At 1,233 K, the XRD pattern shows only the peaks corresponding to the Cu_2Se bulk phase without any peaks related to the $Cu_{1.8}Se$ phase.

We measured the temperature-dependent TE properties of the 3D-printed, heat-treated samples at 873, 1,053 and 1,233 K from room temperature to 1,000 K. The formation of the Se-rich $Cu_{2-x}Se$ phase in our samples enabled control of the hole concentration of the samples because the Cu vacancies in $Cu_{2-x}Se$ are known to act as hole donors (Fig. 5b). Hall measurement results reveal that the hole concentration decreased from 7.27×10^{20} to 3.85×10^{20} cm^{-3} as the heat treatment temperature increased, indicating the controlled formation of the Cu vacancy depending on the sintering temperatures. The hole mobilities of the samples also decrease with increasing sintering temperature. This trend can be understood by considering the defect formation in the sintered samples at higher temperatures.

Room-temperature electrical conductivity gradually decreased with increasing the sintering temperature (Fig. 5c). Meanwhile, the Seebeck coefficient at room temperature increased with increasing the sintering temperature from 873 K to 1,233 K (Fig. 5d). This trend indicated that the Seebeck coefficient were inversely proportional to the carrier concentration[47,48]. The electrical conductivity decreased as a function of temperature for all the samples over the entire temperature range, whereas the Seebeck coefficients were positive. These dependencies agree with the reported trends for Cu_2Se materials and indicate the behaviour of typical heavily doped semiconductors[41,42,49]. The highest power factor of 9.38 μW cm^{-1} K^{-2} was achieved by the 873 K-sintered sample at 1,000 K (Supplementary Fig. 16).

Over the entire temperature range, the samples sintered at higher temperatures exhibited lower thermal conductivities (Fig. 5e). The 1,233 K-sintered sample exhibited the lowest thermal conductivity of 0.33 W m^{-1} K^{-1} at 950 K, which was lower than the reported values of bulk polycrystalline Cu_2Se materials and similar to those of the recently reported state-of-the-art Cu_2Se TE materials. In previous reports, the remarkably low thermal conductivity of Cu_2Se was achieved by strategies to create unique microstructures, such as mosaic nanostructuring[50,51], the fabrication of nanocomposites[52,53], incorporation of carbon allotropes[54–56] and atomic defect engineering[57].

To understand the extremely low thermal conductivity of the 3D-printed Cu_2Se, the sample sintered at 1,233 K was analysed using transmission electron microscopy (TEM). The TEM images (Fig. 5f and Supplementary Fig. 17) clearly show dense array textures in the microstructures. These textures originate from the formation of SFs (Fig. 5g), which is further confirmed by the selected-area electron diffraction pattern (Fig. 5h) that possesses a (004) slip plane. The presence of diffuse streaks surrounding each diffraction pattern provides clear evidence that the microstructure corresponds to an SF in the planar defect[58–60]. Moreover, we observed the formation of dislocation defects surrounded by SFs (Supplementary Fig. 18). In the sample sintered at 873 K, arrays of SFs were partially detected just near the grain boundary. Moreover, the Se-rich $Cu_{1.8}Se$ phase was clearly detected (Supplementary Fig. 19).

The formation of SFs has been widely studied in materials with mixed phases, where a dislocation is created at the phase boundary between the two phases owing to lattice strain, which consequently creates an SF by dislocation propagation[61–64]. The interaction between Cu_2Se particles and Se additive resulted in the formation of Se-rich $Cu_{1.8}Se$ alongside the Cu_2Se matrix phase in our samples (Supplementary Figs. 20 and 21). This intermediate phase can be attributed to lattice strain caused by the lattice mismatch between orthorhombic Cu_2Se and cubic $Cu_{1.8}Se$, leading to the creation of dislocations and dense SFs within the 3D-printed Cu_2Se samples. Notably, at elevated sintering temperatures, the diffusivity of Se ions escalated[65], facilitating their migration into Cu_2Se grains and promoting the development of $Cu_{1.8}Se$ phases in larger regions during the intermediate state. Consequently, this process contributed to the widespread presence of SFs throughout the Cu_2Se grain during subsequent heat treatment. This scenario is supported by the observation of SF arrays in all the grains of the sample sintered at 1,233 K, whereas SFs were observed only at the grain boundary of the sample sintered at 873 K. The enlarged XRD patterns (Supplementary Fig. 20) and TEM results affirmed these observations, revealing peak shifts and heightened lattice strains as sintering temperatures or holding times increased.

Utilizing the Debye–Callaway model encompassing phonon scattering mechanisms such as Umklapp processes, grain boundary scattering, point defects, dislocations, pores and SF scattering, we quantified the attained minimum lattice thermal conductivity (κ_L) (Fig. 5i). Contrary to Umklapp processes, point defects, dislocations and pores primarily impacted low- and high-frequency phonons, showing minimal effect on middle-frequency phonons. Conversely, SFs exhibited substantial phonon scattering reduction across all frequencies, including middle-frequency phonons. Figure 5j demonstrates the accordance between experimental and theoretical data, solidifying the existence of SF-mediated phonon scattering.

The calculated ZT values from the measured electrical and thermal properties reached 2.0 at 950 K for the sample sintered at 1,233 K, outperforming those of the samples sintered at lower temperatures over the entire temperature range. Moreover, this maximum is higher than the values reported for polycrystalline bulk Cu_2Se (ref. 43). Although this value is slightly lower than the recently reported state-of-the-art Cu_2Se (refs. 52–56), to the best of our knowledge, this is the first demonstration of the achievement of higher ZT values in printed TE materials compared with their bulk values (Supplementary Table 2). Further, a thermal cycling test (Supplementary Fig. 22) and the reproducibility test (Supplementary Fig. 23) confirmed the thermal stability and the reproducibility of the 3D-printed samples. Notably, the samples for the reproducibility test were 3D-printed along different printing directions (in-plane, zigzag and cross-plane), indicating the isotropic nature of the TE properties of our samples, unaffected by the printing direction.

Evaluation of power generation of Cu_2Se TE materials

To experimentally validate our designs, we 3D-printed eight distinct geometries of Cu_2Se TE legs that were sandwiched by the Ni diffusion barriers and Cu plate electrodes using Ag paste as the solder (Fig. 6a–f and Supplementary Fig. 24). Under the fixed T_h and convective cooling condition, as the temperature increased, all devices exhibited nearly linear increases in the ΔT and V, and quadratic increases in the P_{max}, indicating the reliability of the measurements (Fig. 6g–i and Supplementary Figs. 25 and 26). Furthermore, the cold-side temperature (T_c) and the resulting ΔT are in good agreement with the simulation results.

Fig. 5 | Optimizing the TE properties of the 3D-printed Cu_2Se by defect engineering. a, XRD spectra of 3D-printed samples sintered at 873, 1,053 and 1,233 K. **b**, Room-temperature hole concentrations and mobilities of the Cu_2Se samples sintered at 873, 1,053 and 1,233 K. **c**–**e**, Temperature-dependent electrical conductivities (**c**), Seebeck coefficients (**d**) and thermal conductivities (**e**) of the Cu_2Se samples sintered at 873 K, 1,053 K and 1,233 K. **f**–**h**, Field emission TEM images at low (**f**) and high (**g**) magnifications of the 3D-printed Cu_2Se grain sintered at 1,233 K. The yellow arrow in **c** indicates SFs. **h**, The selected-area electron diffraction image of the TEM image. **i**, Full frequency spectrum of the phonon scattering effect in the 3D-printed Cu_2Se. The interplay of Umklapp (U), grain boundary (GB), point defect (PD) and dislocation (DC + DS) scattering can reduce the spectral thermal conductivity exclusively at specific low- and high-frequency intervals. The red-shaded area in **i** represents the reduction in spectral thermal conductivity due to SFs only. **j**, Temperature-dependent lattice thermal conductivities of 3D-printed Cu_2Se samples sintered at 873, 1,053 and 1,233 K. The dashed and dotted lines represent the simulated and measured data, respectively.

https://doi.org/10.1038/s41560-024-01589-5

Notably, at T_h of 873 K, the hourglass exhibited a T_c of 378.6 K among those observed in other geometries (Supplementary Fig. 26). Correspondingly, the V mirrored the trends in ΔT. Consequently, the hourglass showed the markedly enhanced P_{max} of 25.9 mW, approximately 2.1 times higher than those exhibited by the cuboid. Moreover, the enhancement in the η achieved by the hourglass was even more pronounced than

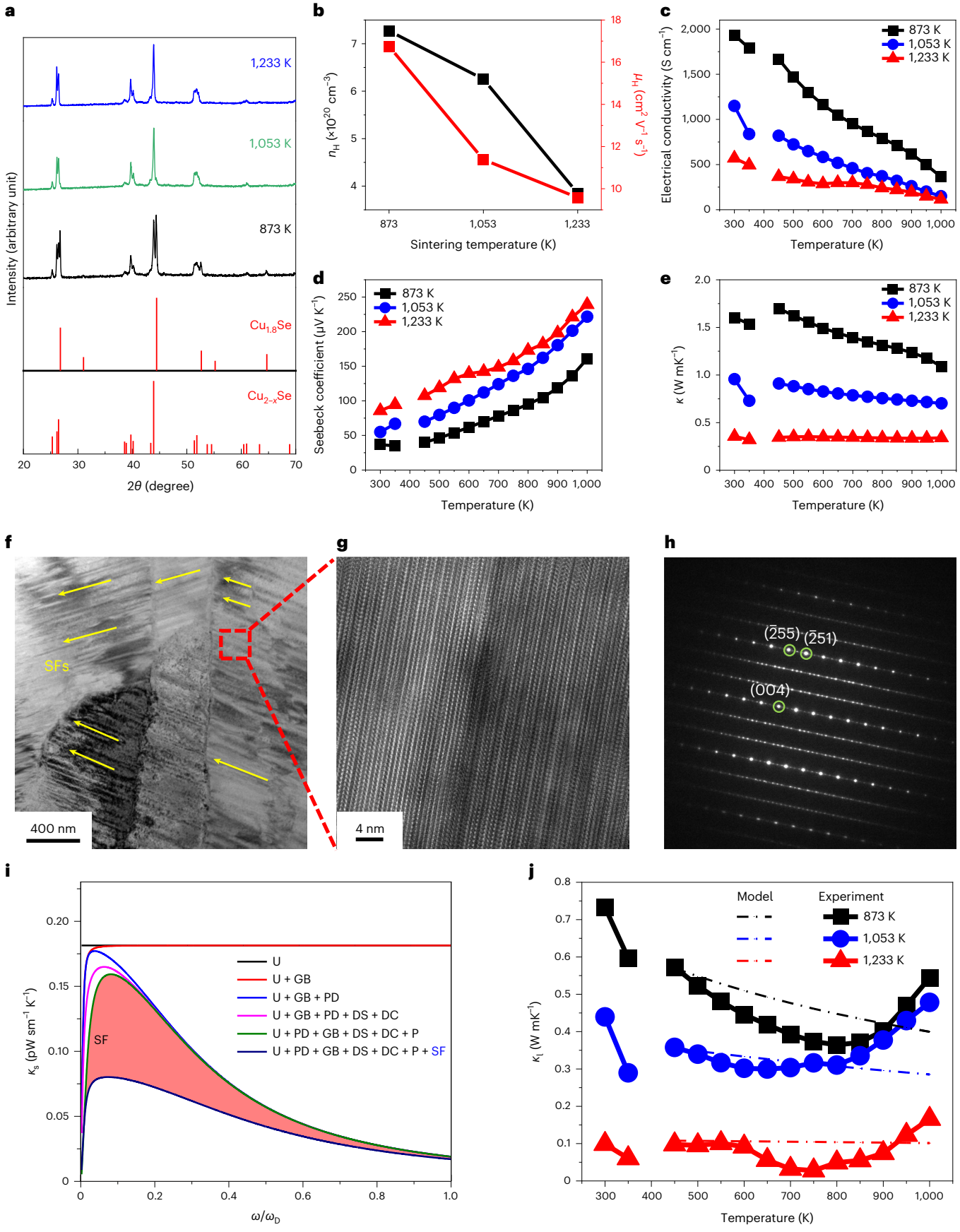

https://doi.org/10.1038/s41560-024-01589-5

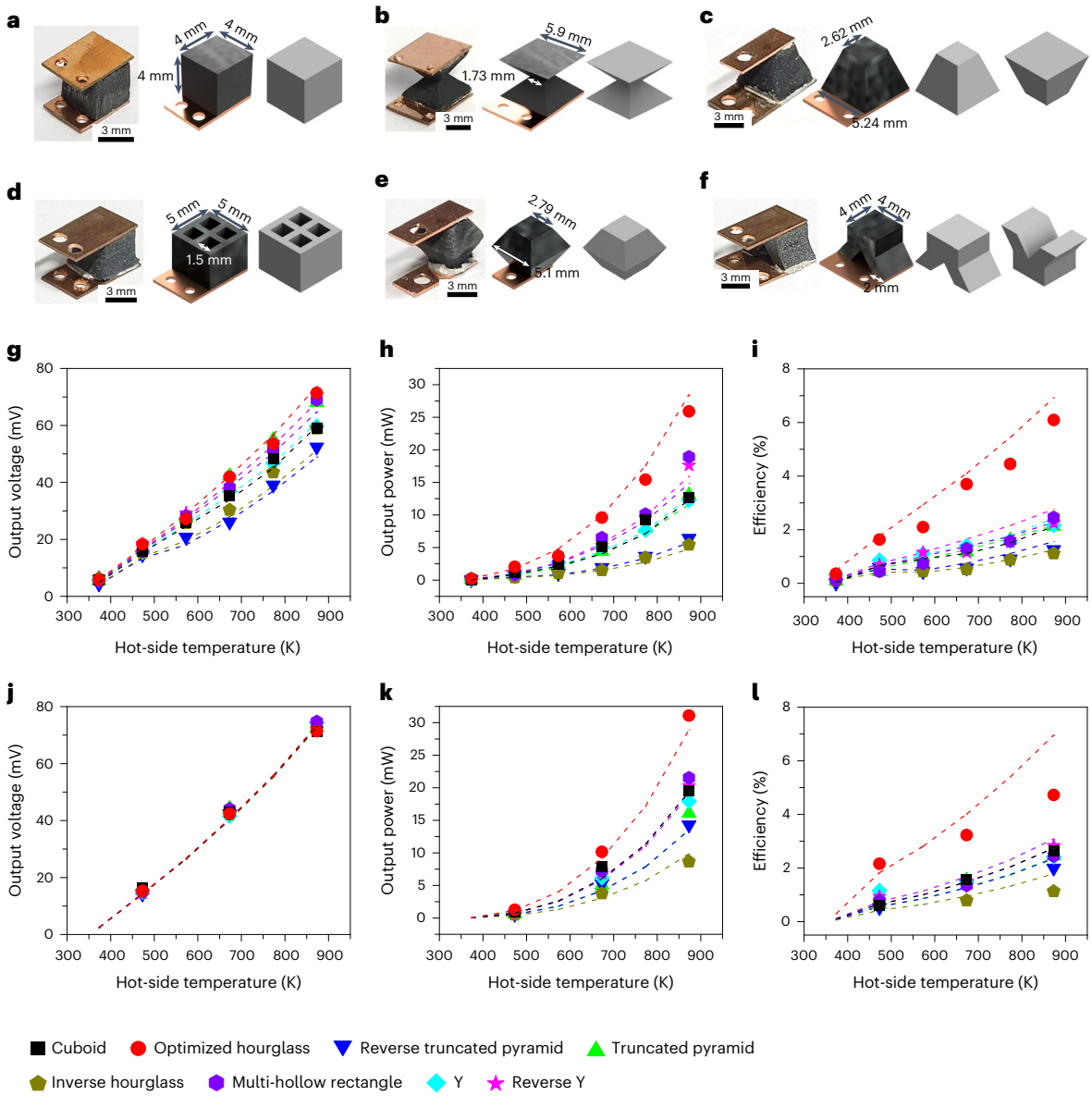

Fig. 6 | Power-generating performances of 3D-printed Cu_2Se devices. **a**–**f**, Photographs and 3D illustrated models of TE devices chipped with cuboid- (**a**), optimized hourglass- (**b**), truncated pyramid- (**c**), multi-hollow rectangle- (**d**), reverse hourglass- (**e**) and Y- (**f**) shaped Cu_2Se TE legs. **g**–**i**, Output voltages (**g**), powers (**h**) and efficiencies (**i**) as a function of the hot-side temperature of the 3D-printed Cu_2Se TE devices under the fixed T_h condition. **j**–**l**, Output voltages (**j**), powers (**k**) and efficiencies (**l**) as a function of the hot-side temperature of the 3D-printed Cu_2Se TE devices under the fixed ΔT condition. The points and dashed lines in the graphs are the measured and simulated data, respectively, that were determined by FEM simulations.

their P_{max}, reaching 6.1% at the T_h of 873 K. This η was 3.6 times greater than that of the cuboid, respectively (Fig. 6i). Such enhancements are ascribed to the larger ΔT created in comparison with other designs at equivalent T_h, which is a consequence of the increased R_{th} due to the geometric parameters, as well as the expanded cooling surfaces.

In addition, under the fixed ΔT condition, all samples exhibit nearly identical output voltages across measurement temperatures (Fig. 6j–l). The P_{max} of each leg was primarily influenced by its R_{el}, with the hourglass demonstrating the lowest R_{el}, attributable to the larger contact surface area with the electrodes. Accordingly, the optimized hourglass shows the highest P_{max} of 29.75 mW, surpassing other geometries by approximately 1.5 times, relative to the cuboid. Moreover, the η/P_{max} of the hourglass was superior compared with that of the cuboid, indicating that an equivalent ΔT could be generated with a reduced Q_h in more complex geometries characterized by higher geometric parameters and consequent R_{th}. These results demonstrate the impact of the geometry for enhancing the power-generating performance under diverse working conditions.

These experimental results are in concordance with the simulation results in the 3D plots under the various thermal environment conditions (Fig. 2a–e), corresponding to the constant cooling h of 200 W m^{-2} K^{-1} and the heating and cooling h of infinite (Supplementary Figs. 27 and 28). Such consistency demonstrates the effect of geometry on the power-generating efficiency of the devices under various working conditions.

Discussion

We demonstrated the feasibility of the design and 3D printing strategy for non-cuboid geometries of Cu_2Se TE materials for more efficient thermal energy harvesters. We developed 3D FEMs for the library of geometries of TE legs that allowed us to comparatively optimize the geometries of the TE legs with respect to the geometric parameter for creating a larger

thermal resistance, resulting in a higher output power and efficiency. Moreover, we demonstrated the controlled formation of atomic defects in 3D-printed Cu_2Se by induced lattice strain in the Cu_2Se grains, where a high density of SF arrays was created in the entire grain. Such defect engineering allowed us to substantially reduce the thermal conductivity and enhance the ZT values up to 2.0. The experimental validation of the FEM design by 3D printing fabrication and evaluation of the TE materials showed excellent agreement with the predicted power-generating performances, where the hourglass geometry exhibited noticeably higher output power and efficiencies than the other geometries. Our design strategy for the non-cuboid geometry of a TE material provides a way to overcome the intrinsic trade-off between the electrical and thermal transport in a device. For instance, the numerical simulation shows that the ratio of electrical to thermal current density—a critical factor for maximizing efficiency—can be tuned by the geometry (Supplementary Discussion 5 and Supplementary Fig. 29). In addition, this strategy can be easily applied to other TE materials, as evidenced with BiSbTe (Supplementary Fig. 5), and functional properties of materials, such as mechanical, optical and catalytic properties. Despite the anticipated mechanical vulnerability of the hourglass structure (Supplementary Fig. 12), the incorporation of mechanically robust fillers or the implementation of a 3D metastructure design can enhance the durability at the device level. Our approach will unveil a new way to enhance the efficiency of TE devices, which ultimately contributes to future electricity supplies.

Methods

Materials

Chemicals used in this research were purchased from the following suppliers: ethylenediamine (>99.5% pure), glycerol (>99.5% pure) and ethanethiol (>97% pure) from Aldrich Chemical; Cu (99.9%) powder and Se (99.999%) powder for high-energy ball milling from Alfa Aesar and 5N Plus, respectively; and isopropanol (99.5%) and Se (99.999%) powder for the synthesis of Se polyanion from Samchun Chemicals and Alfa Aesar, respectively. The chemicals and elements were used as received without further purification.

Synthesis of 3D-printable all-inorganic $Cu_{2-x}Se$-based ink

The entire procedure was conducted under N_2 atmosphere. To synthesize Cu_2Se powder, Cu and Se powder with the stoichiometric ratio of Cu_2Se were high-energy ball-milled (SPEX, 8000M Mixer/Mill) for 200 min. The resulting powder was sieved to eliminate particles larger than 45 µm. The Se polyanion additive was prepared with the following process: dissolving 0.5 g of Se powder in cosolvent of 0.5 ml of ethanethiol and 4.5 ml of ethylenediamine at room temperature with vigorous stirring. After 72 h, 5 ml of Se dissolved solution was mixed with 37.5 ml of isopropanol and centrifugated for 10 min at 7,715g to precipitate the Se polyanion from the dissolved solution. The precipitate was vacuum-dried for 1 h after discarding the supernatant. Cu_2Se-based ink was prepared by dispersing 2 or 3 g of ball-milled Cu_2Se powder, 1 or 1.5 g of dried Se polyanion, and 2.5 g of glycerol for 2 h in a planetary centrifugal mixer (ARM-100, Thinky). To ensure successful homogenization, five to seven zirconium oxide grinding balls with a 5 mm diameter were introduced into the mixing process.

Rheological characterizations of $Cu_{2-x}Se$-based inorganic ink

The rheological properties of the Cu_2Se inorganic ink were assessed at room temperature using a rotational rheometer (Haake MARS III, Thermo Scientific) with a coaxial cylinder geometry. Frequency sweep tests were performed at a constant stress of 1 Pa, while stress sweep tests were conducted at frequencies of 1 rad s^{-1} and stress values ranging from 0.005 to 300 Pa.

3D printing and heat treatment process of Cu_2Se

Three-dimensional printing was conducted using a home-built extrusion-based 3D printer with programmable temperature and pressure control. The synthesized ink was loaded into a 5 ml syringe (Saejong), which was fitted with a metal nozzle having an inner diameter of 340 µm. The design software was used to print the ink in layers of parallel lines, with each layer developed perpendicular to the previous one. The printing process was carried out at room temperature, with a 1 s interval between each layer deposition. The as-printed sample was dried at 423 K for 5 h and subsequently annealed under a nitrogen atmosphere at 873, 1,053 and 1,233 K for 1–13 h.

Microstructure characterization of 3D-printed Cu_2Se

The Olympus BX51M was used to capture the optical microscopy image. The field-effect SEM (Nova-NanoSEM230, FEI and S-4800 Hitachi High-Technologies) operated at 30 kV was used to obtain the SEM images. The XRD patterns were obtained by the Rigaku D/Max2500 V diffractometer with a Cu-rotating anode X-ray source (λ = 0.15418 nm) operating at 40 kV and 30 mA. The reference peaks of $Cu_{2-x}Se$ and $Cu_{1.8}Se$ were determined by comparison with the references of JCPDS: 00-047-1448 and 01-073-8642, respectively. The TEM specimens were prepared using focused ion beam milling (NX5000, Hitachi), and the FE-TEM characterization was performed using the Titan G2 ChemiSTEM Cs Probe from FEI company.

Measurement of TE properties

The temperature-dependent electrical conductivity and Seebeck coefficient were measured using a commercial equipment (SBA 458 Nemesis, Netzsch) under argon atmosphere in the temperature range of 300 K to 1,000 K. The thermal conductivity of the 3D-printed samples was estimated using the formula $\kappa = \rho C_p D$, where κ is the thermal conductivity, ρ is the density, C_p is the specific heat capacity and D is the thermal diffusivity, which was measured using laser flash analysis (LFA 467HT, Netzsch) in the same temperature range as the electrical conductivity. The maximum equipment error range for thermal diffusivity, considering radiation heat loss, is limited to 3%. The density of the samples was obtained by measuring their weight and volume. The specific heat capacity was calculated using the Dulong–Petit equation. The maximum equipment error range for thermal diffusivity measurement was 3%. All the measurements were conducted with the 3D-printed Cu_2Se made from Cu_2Se ink containing 5 g of glycerol medium, 4 g of ball-milled Cu_2Se powder and 2 g of Se polyanion additive. Room carrier concentrations and mobility were evaluated using an equipment of HCS-1, LINSEIS, capable of generating dual opposing magnetic fields of ±0.7 T. TE properties are slightly changed during the process of optimizing the heat treatment duration at the sintering temperature of 1,233 K. (Supplementary Figs. 30 and 31). Owing to the phase transition, the TE properties of the Cu_2Se samples at around 400 K fluctuated, not displayed in Figs. 1b and 5 ref. 33.

Optimizing TE generator design

A 3D FEM was developed using the commercial software COMSOL Multiphysics to calculate the temperature difference, output voltage and power of the TE device. The dimensions of the shapes used in the TE leg are shown in Fig. 1a, and the volume of the TE material used is 64 mm^3 with a height of 4 mm. The material properties of the used TE material are depicted in Fig. 5b–e. The electrical conductivity, thermal conductivity and Seebeck coefficient of Cu_2Se used in the FEM were interpolated with cubic splines based on the measured properties. To evaluate the performance enhancement attributable to the alteration in geometry within a suitable temperature range, the boundary conditions were established as follows: a fixed temperature of 873 K or varying convection coefficients on the hot side with an ambient temperature of 873 K, and a fixed temperature of 350 K or varying convection coefficients on the cold side with an ambient temperature of 300 K. Adiabatic conditions were applied to the exterior sides. In the TE device, the electrical potential (V_{oc}) was calculated by applying electrical ground to the top surface at open circuit and the current (I_{sc}) was

calculated at short circuit to obtain the electrical resistance ($R = V_{oc}/I_{sc}$). The maximum output power (P_{max}) was calculated using $P_{max} = V_{oc}^2/4R$. The η was computed via $\eta = P_{max}/Q_h = P_{max}/(P_{max} + Q_c)$, where Q_h and Q_c are the heat transfer rates from a heat source and to the cold side, respectively. The cross-sectional area of the electrodes, which has a thickness of 1 mm, is the same as those of the boundary surface of the TE leg, except for the narrow side of the truncated pyramid which uses electrode of the same size as the wider side. The solder layer between the electrodes and the TE leg was modelled with a thickness of 0.1 mm, and the properties of Ag paste were applied: electrical conductivity (σ) of 5×10^5 S m^{-1}, Seebeck coefficient (S) of 0 V K^{-1}, thermal conductivity (κ) of 9.1 W m^{-1} K^{-1} and specific heat capacity (C_p) of 167 J kg^{-1} K^{-1}. The contact resistance (R_c) was applied to interlayer between the electrode and TE leg with the contact resistivity of 4.88×10^5 Ωm^2, which is based on the measured values (Supplementary Fig. 3). The value of h, 200 W m^{-2} K^{-1}, was identified as the optimal parameter when water circulating cooling was employed[33].

Fabrication and power measurement of Cu_2Se TE devices

Copper electrodes were prepared in suitable dimensions and thickness of 0.3 mm for three distinct geometries of Cu_2Se legs presented in Fig. 5a–c. Nickel layers, each 300 nm in thickness, were deposited on both the top and bottom surfaces of the 3D-printed Cu_2Se TE legs through a sputtering process. Following this metallization, the samples were connected to copper electrodes using silver paste (Pyro-Duct 597-A, Aremco). The output power was measured under a temperature difference using a 70 mm by 15 mm ceramic heater as the heat source and a water-circulating chiller. To prevent thermal convection and radiation, glass fabric was wrapped around the hot plate and 3D-printed TE devices. Temperature changes were monitored with K-type thermocouples connected to a Keithley 2000 multimeter. To avoid unintended oxidation and air convection, the entire evaluation was performed in a vacuum chamber (Supplementary Fig. 32).

Data availability

All data generated or analysed during this study are included in the published article and its Supplementary Information. Source data are provided with this paper.

Code availability

The COMSOL Multiphysics codes generated for this work have been uploaded to Zenodo at https://zenodo.org/records/12154029 (ref. 66).

References

1. Brockway, P. E., Owen, A., Brand-Correa, L. I. & Hardt, L. Estimation of global final-stage energy-return-on-investment for fossil fuels with comparison to renewable energy sources. *Nat. Energy* **4**, 612–621 (2019).
2. Yang, H., Huang, X., Westervelt, D. M., Horowitz, L. & Peng, W. Socio-demographic factors shaping the future global health burden from air pollution. *Nat. Sustain.* **6**, 58–68 (2022).
3. Barnes, P. W. et al. Ozone depletion, ultraviolet radiation, climate change and prospects for a sustainable future. *Nat. Sustain.* **2**, 569–579 (2019).
4. Habert, G. et al. Environmental impacts and decarbonization strategies in the cement and concrete industries. *Nat. Rev. Earth Environ.* **1**, 559–573 (2020).
5. Forman, C., Muritala, I. K., Pardemann, R. & Meyer, B. Estimating the global waste heat potential. *Renew. Sust. Energ. Rev.* **57**, 1568–1579 (2016).
6. Jouhara, H. et al. Waste heat recovery technologies and applications. *Therm. Sci. Eng. Prog.* **6**, 268–289 (2018).
7. Bell, L. E. Cooling, heating, generating power, and recovering waste heat with thermoelectric systems. *Science* **321**, 1457–1461 (2008).
8. DiSalvo, F. J. Thermoelectric cooling and power generation. *Science* **285**, 703–706 (1999).
9. He, J. & Tritt, T. M. Advances in thermoelectric materials research: Looking back and moving forward. *Science* **357**, eaak9997 (2017).
10. Snyder, G. J. & Toberer, E. S. Complex thermoelectric materials. *Nat. Mater.* **7**, 105–114 (2008).
11. Li, J.-F., Liu, W.-S., Zhao, L.-D. & Zhou, M. High-performance nanostructured thermoelectric materials. *NPG Asia Mater.* **2**, 152–158 (2010).
12. He, S., Lehmann, S., Bahrami, A. & Nielsch, K. Current state-of-the-art in the interface/surface modification of thermoelectric materials. *Adv. Energy Mater.* **11**, 2101877 (2021).
13. Shittu, S., Li, G., Zhao, X. & Ma, X. Review of thermoelectric geometry and structure optimization for performance enhancement. *Appl. Energy* **268**, 115075 (2020).
14. LeBlanc, S. Thermoelectric generators: linking material properties and systems engineering for waste heat recovery applications. *SMT* **1-2**, 26–35 (2014).
15. Zhang, Q. et al. Realizing a thermoelectric conversion efficiency of 12% in bismuth telluride/skutterudite segmented modules through full-parameter optimization and energy-loss minimized integration. *Energy Environ. Sci.* **10**, 956–963 (2017).
16. He, Z.-Z. A coupled electrical-thermal impedance matching model for design optimization of thermoelectric generator. *Appl. Energy* **269**, 115037 (2020).
17. Xing, Y. et al. High-efficiency half-Heusler thermoelectric modules enabled by self-propagating synthesis and topologic structure optimization. *Energy Environ. Sci.* **12**, 3390–3399 (2019).
18. Qiu, P. et al. High-efficiency and stable thermoelectric module based on liquid-like materials. *Joule* **3**, 1538–1548 (2019).
19. Xing, T. et al. High efficiency GeTe-based materials and modules for thermoelectric power generation. *Energy Environ. Sci.* **14**, 995–1003 (2021).
20. Skomedal, G. et al. Design, assembly and characterization of silicide-based thermoelectric modules. *Energy Convers. Manag.* **110**, 13–21 (2016).
21. Erturun, U., Erermis, K. & Mossi, K. Effect of various leg geometries on thermo-mechanical and power generation performance of thermoelectric devices. *Appl. Therm. Eng.* **73**, 128–141 (2014).
22. Ibrahim, A., Rahnamayan, S., Vargas Martin, M. & Yilbas, B. Multi-objective thermal analysis of a thermoelectric device: Influence of geometric features on device characteristics. *Energy* **77**, 305–317 (2014).
23. Menon, A. K., Meek, O., Eng, A. J. & Yee, S. K. Radial thermoelectric generator fabricated from n- and p-type conducting polymers. *J. Appl. Polym. Sci.* **134**, 44060 (2017).
24. Ali, H., Sahin, A. Z. & Yilbas, B. S. Thermodynamic analysis of a thermoelectric power generator in relation to geometric configuration device pins. *Energy Convers. Manag.* **78**, 634–640 (2014).
25. Fabián-Mijangos, A., Min, G. & Alvarez-Quintana, J. Enhanced performance thermoelectric module having asymmetrical legs. *Energy Convers. Manag.* **148**, 1372–1381 (2017).
26. Thimont, Y. & LeBlanc, S. The impact of thermoelectric leg geometries on thermal resistance and power output. *J. Appl. Phys.* **126**, 095101 (2019).
27. Şişik, B. & LeBlanc, S. The influence of leg shape on thermoelectric performance under constant temperature and heat flux boundary conditions. *Front. Mater.* **7**, 595955 (2020).
28. Jo, S., Choo, S., Kim, F., Heo, S. H. & Son, J. S. Ink processing for thermoelectric materials and power-generating devices. *Adv. Mater.* **31**, e1804930 (2019).
29. Kim, F. et al. 3D printing of shape-conformable thermoelectric materials using all-inorganic Bi2Te3-based inks. *Nat. Energy* **3**, 301–309 (2018).

30. Yang, S. E. et al. Composition-segmented BiSbTe thermoelectric generator fabricated by multimaterial 3D printing. *Nano Energy* **81**, 105638 (2021).
31. Lee, J. et al. Doping-Induced viscoelasticity in PbTe thermoelectric inks for 3D printing of power-generating tubes. *Adv. Energy Mater.* **11**, 2100190 (2021).
32. Kim, F. et al. Direct ink writing of three-dimensional thermoelectric microarchitectures. *Nat. Electron.* **4**, 579–587 (2021).
33. Choo, S. et al. Cu_2Se-based thermoelectric cellular architectures for efficient and durable power generation. *Nat. Commun.* **12**, 3550 (2021).
34. Tarancón, A. et al. 2022 roadmap on 3D printing for energy. *J. Phys. Energy* **4**, 011501 (2022).
35. Zeng, M. et al. Printing thermoelectric inks toward next-generation energy and thermal devices. *Chem. Soc. Rev.* **51**, 485–512 (2022).
36. Burton, M., Howells, G., Atoyo, J. & Carnie, M. Printed thermoelectrics. *Adv. Mater.* **34**, e2108183 (2022).
37. Biswas, K. et al. Thermoelectric materials science and technology toward applications. *Appl. Phys. Lett.* **121**, 070401 (2022).
38. Kim, K. S. et al. Direct observation of inherent atomic-scale defect disorders responsible for high-performance $Ti_{1-x}Hf_xNiSn_{1-y}Sb_y$ half-Heusler thermoelectric alloys. *Adv. Mater.* **29**, 1702091 (2017).
39. Zhao, K., Qiu, P., Shi, X. & Chen, L. Recent advances in liquid-like thermoelectric materials. *Adv. Funct. Mater.* **30**, 1903867 (2019).
40. Powell, A. V. Recent developments in Earth-abundant copper-sulfide thermoelectric materials. *J. Appl. Phys.* **126**, 100901 (2019).
41. Liu, W. D., Yang, L., Chen, Z. G. & Zou, J. Promising and eco-friendly Cu_2X-based thermoelectric materials: progress and applications. *Adv. Mater.* **32**, e1905703 (2020).
42. Zhang, Z. et al. Cu2Se-Based liquid-like thermoelectric materials: looking back and stepping forward. *Energy Environ. Sci.* **13**, 3307–3329 (2020).
43. Wei, T.-R. et al. Copper chalcogenide thermoelectric materials. *Sci. China Mater.* **62**, 8–24 (2018).
44. Liu, H. et al. Copper ion liquid-like thermoelectrics. *Nat. Mater.* **11**, 422–425 (2012).
45. Al-Merbati, A. S., Yilbas, B. S. & Sahin, A. Z. Thermodynamics and thermal stress analysis of thermoelectric power generator: Influence of pin geometry on device performance. *Appl. Therm. Eng.* **50**, 683–692 (2013).
46. Schroder, D. K. *Semiconductor Material and Device Characterization* (John Wiley & Sons, 2005).
47. Sootsman, J. R., Chung, D. Y. & Kanatzidis, M. G. New and old concepts in thermoelectric materials. *Angew. Chem. Int. Ed. Engl.* **48**, 8616–8639 (2009).
48. Dresselhaus, M. S. et al. New directions for low-dimensional thermoelectric materials. *Adv. Mater.* **19**, 1043–1053 (2007).
49. Qiu, P., Shi, X. & Chen, L. Cu-based thermoelectric materials. *Energy Stor. Mater.* **3**, 85–97 (2016).
50. Zhao, K. et al. High thermoelectric performance and low thermal conductivity in $Cu_{2-y}S_{1/3}Se_{1/3}Te_{1/3}$ liquid-like materials with nanoscale mosaic structures. *Nano Energy* **42**, 43–50 (2017).
51. Zhao, K. et al. Extremely low thermal conductivity and high thermoelectric performance in liquid-like $Cu_2Se_{1-x}S_x$ polymorphic materials. *J. Mater. Chem. A* **5**, 18148–18156 (2017).
52. Zhou, Z. et al. Compositing effects for high thermoelectric performance of Cu_2Se-based materials. *Nat. Commun.* **14**, 2410 (2023).
53. Olvera, A. A. et al. Partial indium solubility induces chemical stability and colossal thermoelectric figure of merit in Cu_2Se. *Energy Environ. Sci.* **10**, 1668–1676 (2017).
54. Zhao, L. et al. Significant enhancement of figure-of-merit in carbon-reinforced Cu_2Se nanocrystalline solids. *Nano Energy* **41**, 164–171 (2017).
55. Nunna, R. et al. Ultrahigh thermoelectric performance in Cu_2Se-based hybrid materials with highly dispersed molecular CNTs. *Energy Environ. Sci.* **10**, 1928–1935 (2017).
56. Li, M. et al. Ultra-high thermoelectric performance in graphene incorporated Cu_2Se: role of mismatching phonon modes. *Nano Energy* **53**, 993–1002 (2018).
57. Mao, T. et al. Enhanced thermoelectric performance and service stability of Cu_2Se via tailoring chemical compositions at multiple atomic positions. *Adv. Funct. Mater.* **30**, 1908315 (2019).
58. Ming, H. et al. Creating high-dense stacking faults and endo-grown nanoneedles to enhance phonon scattering and improve thermoelectric performance of Cu_2SnSe_3. *Nano Energy* **100**, 107510 (2022).
59. Poddar, D., Ghosh, C., Bhattacharya, B. & Singh, V. K. Development of high ductile ultra high strength structural steel through stabilization of retained austenite and stacking fault. *Mater. Sci. Eng. A* **762**, 138079 (2019).
60. Chen, D. J. et al. Weak strengthening effect of the precipitated lamellar phase in the homogenized Mg-8Gd-4Y-1.6Zn-0.5Zr (wt%) alloy followed by furnace cooling. *Mater. Sci. Eng. A* **744**, 1–9 (2019).
61. Salamania, J. et al. High-resolution STEM investigation of the role of dislocations during decomposition of $Ti_{1-x}Al_xN_y$. *Scr. Mater.* **229**, 115366 (2023).
62. Liu, X. S. et al. Spinodal decomposition induced nanoprecipitates strengthened CoCrNi-base medium entropy alloy. *Mater. Sci. Eng. A* **822**, 141674 (2021).
63. Mangel, S., Houben, L. & Bar Sadan, M. The effect of atomic disorder at the core–shell interface on stacking fault formation in hybrid nanoparticles. *Nanoscale* **8**, 17568–17572 (2016).
64. Su, R. et al. Deformation mechanisms in FCC Co dominated by high-density stacking faults. *Mater. Sci. Eng. A* **736**, 12–21 (2018).
65. Guldi, R. L., Walpole, J. N. & Rediker, R. H. Diffusion of lead and selenium in lead selenide. *J. Appl. Phys.* **44**, 4896–4907 (1973).
66. Lee, J. Source files of COMSOL in article: Geometric design of Cu2Se-based thermoelectric materials for enhancing power generation. *Zenodo* https://doi.org/10.5281/zenodo.12154029 (2024).

Acknowledgements

This work was supported by the National Research Foundation of Korea (NRF) grant funded by the Korea government (MSIT) (NRF-2022R1A2C3009129 and NRF-2022M3H4A1A04076667). B.Ş. and S.L. acknowledge the United States National Science Foundation (award number CMMI-1943104). We thank B. Ryu for helpful discussion.

Author contributions

S.C. and J.L. contributed equally to this work. S.C., J.L., B.Ş., S.L. and J.S.S. designed the experiments, analysed the data and wrote the paper. S.C., J.L., S.E.Y. and S.J. carried out the synthesis and basic characterization of materials. S.-J.J. and S.K.K. carried out calculation of modelled lattice thermal conductivities. K.K. and H.G.C. performed the characterization of rheological properties. C.N. and S.A. performed the characterization of thermal conductivities. H.L. performed the characterization of TEM analysis. S.C. carried out the fabrication and measurement of TEGs. J.L., B.Ş. and S.L. performed the simulation studies. All authors discussed the results and commented on the manuscript.

Competing interests

The authors declare no competing interests.

Additional information

Supplementary information The online version contains supplementary material available at https://doi.org/10.1038/s41560-024-01589-5.

Correspondence and requests for materials should be addressed to Saniya LeBlanc or Jae Sung Son.

Peer review information *Nature Energy* thanks Matthew Burton, Kornelius Nielsch, Ady Suwardi and the other, anonymous, reviewer for their contribution to the peer review of this work.

[1]Department of Chemical Engineering, Pohang University of Science and Technology, Pohang, Republic of Korea. [2]Department of Mechanical and Aerospace Engineering, The George Washington University, Washington, DC, USA. [3]Samsung Research, Samsung Electronics, Seoul, Republic of Korea. [4]Electronic Materials Research Center, Korea Institute of Science and Technology, Seoul, Republic of Korea. [5]Nanomaterials Research Division, Korea Institute of Materials Science, Changwon, Republic of Korea. [6]Department of Nuclear Engineering, Ulsan National Institute of Science and Technology, Ulsan, Republic of Korea. [7]Department of Materials Science and Metallurgical Engineering, Kyungpook National University, Daegu, Republic of Korea. [8]Department of Materials Science and Engineering, Ulsan National Institute of Science and Technology, Ulsan, Republic of Korea. [9]KU-KIST Graduate School of Converging Science and Technology, Korea University, Seoul, Republic of Korea. [10]These authors contributed equally: Seungjun Choo, Jungsoo Lee. ✉e-mail: sleblanc@gwu.edu; sonjs@postech.ac.kr